7168 *Macromolecules* **2009**, *42*, 7168–7183
DOI: 10.1021/ma802555r

Macromolecules
ARTICLE

Slip-Link Simulations of Entangled, Finitely Extensible, Wormlike Chains in Shear Flow

Ajey Dambal,[†] Amit Kushwaha,[‡] and Eric S. G. Shaqfeh*[,†,‡]

[†]*Department of Chemical Engineering, Stanford University, Stanford, California 94025, and* [‡]*Department of Mechanical Engineering, Stanford University, Stanford, California 94025*

Received November 13, 2008; Revised Manuscript Received August 10, 2009

ABSTRACT: We present computer simulations of entangled finitely extensible wormlike chains, including real space chain coupling, in shearing flows. Extending existing simulation techniques, we examine the microstructure of such concentrated polymer systems at both equilibrium and in "fast" shear flows and compare our simulation results with experimental single molecule data for DNA and with bulk rheological measurements. At equilibrium we verify that our simulation technique predicts that the longest relaxation time of the system scales as the number of entanglements to the 3.4 power. Time traces of polymer conformation near equilibrium show fluctuations not only in the flow and gradient directions but also in the vorticity direction as well. At stronger flow rates, we demonstrate the existence of large stretching in the flow-gradient plane coupled to rotational fluctuations which result in polymer tumbling. Under such nonequilibrium flows, we find excellent agreement with single molecule data with regard to the configurational variability of individual molecules for $\dot{\gamma}\tau_R \leq 5$. Both experiments and our simulation data show that chain extension exhibits a wide range of values with maximum extension exceeding 40%. Furthermore, histograms of chain orientation, measured via simulations, are symmetric around 45° and then become skewed toward 0° as the flow strength is increased. However, even under relatively fast flows, the average angle decreases only modestly, and thus strong alignment is never observed. Also in agreement with single molecule data is our simulated variation of the power spectral density of chain size projected in the flow direction, which decays as ω^m where $m \sim -15$ and $m = -2$ for slow and fast flows, respectively. Finally, our simulations are able to predict the onset of a plateau in shear stress for $\tau_D^{-1} < \dot{\gamma} < \tau_R^{-1}$ and also a dip in the linear viscoelastic loss modulus at intermediate frequencies, both classic signatures of entanglement. Our shear stress results are in quantitative agreement with experimental rheological data for T4-DNA. We find that the size of the polymer in the flow and the gradient directions are relatively constant in the range of flow rates corresponding to the shear stress plateau. Only upon the imposition of higher shear rates, when the shear stresses exhibit an upturn after the plateau, do the two size measures display significant variations. These "frozen" changes in the size and orientation of the chains are the microscale cause of the shear stress plateau in our simulations.

1. Introduction

An initial theoretical formulation to understand entangled polymer dynamics was not achieved until the 1970s—years after the development of dilute polymer models by Rouse and Zimm.[1,2] The early work by Doi, Edwards, and deGennes on the mechanics of concentrated polymer systems were based on the "tube" model[3]—an assumption that at high concentrations polymer chains moved as though they were confined to a tubelike region defined by their neighboring chains. Being confined, the motion of a chain was severely restricted in the direction perpendicular to its backbone relative to motion parallel to its contour. As the chain moved back and forth along its contour, its ends freely chose a random orientation, and thus this snakelike motion—dubbed "reptation" by deGennes—eventually led to the chain adopting a completely new conformation after some characteristic time. Realizing this time scale to be related to the amount of the original confining tube that is "remembered" at some future time t, Doi and Edwards were able to reproduce deGennes' estimate of the characteristic time, using a diffusion equation. This time scale, τ_D, is now commonly called the "disengagement" time. Using this reptation-based model, Doi and Edwards were able to predict entangled polymer/melt properties such as chain diffusivity, shear stress growth, and so forth.[3] This success, primarily limited to slow flows, did not carry over to cases with strong deformations. At higher deformation rates, where the polymer orientation was significantly perturbed by flow, the theory's predictions of the shear viscosity $\eta_s \sim \dot{\gamma}^{-3/2}$, where $\dot{\gamma}$ is the imposed shear rate, was found to be incompatible with experimental observations.

The problem of excessive shear thinning was quickly attributed to the instantaneous stretch and relaxation process, which was assumed by the original Doi–Edwards (DE) model. Marrucci and Grizzuti included segmental stretch into the DE framework, but unfortunately it was revealed that this addition did not alleviate the excessive shear shinning.[4,5] The reason lies in the fact that chain stretch becomes significant only when $\dot{\gamma}\tau_R \sim O(1)$. At large entanglement number, Z_0, the Rouse time is much smaller than the disengagement time ($\tau_D/\tau_R = 3Z_0$), forcing chain stretch to be relatively unimportant when the solution starts to shear thin, $\dot{\gamma}\tau_D \sim O(1)$. Despite this setback, the inclusion of chain stretch significantly improved predictions of entangled phenomena in fast flows. However, the theoretical problem of understanding the shear stress plateau remained.

Another possible solution to this problem lay in a concept known as "constraint renewal", which had previously been

---

*To whom correspondence should be addressed. E-mail: esgs@stanford.edu.

researched by Graessley[6] and Viovy.[7] This phenomenon is motivated by the realization that the entire polymer network is acted upon by the same forces that are felt by any given test polymer. Thus, the polymers that confine a given test chain also undergo similar dynamics as the test chain itself. Such a picture implies that the confining "tube" cannot be treated as a static entity since the network itself is time dependent. This stochastic process of imposing new constraints and destroying existing constraints in the system was termed "constraint renewal". Graessley tackled this problem at near equilibrium by modeling the constraints as entities having a finite lifetime.[6] In contrast, Viovy et al. examined this constraint release picture in cases involving large deformations away from equilibrium, for example in cases where chains are initially stretched and must relax back to an equilibrated length.[7]

Nevertheless, the effect of flow on constraint release was not actively examined until the 1990s when Marrucci accounted for the flow's effect on constraints by modifying the terminal relaxation time itself.[8] The idea behind this modification was that the ambient flow would convect constraints along with it and thus allow entangled chains to relax on a time scale which depends on the imposed strain rate in nonequilibrium settings and reduces to the disengagement time at equilibrium.[8] This model, although ad hoc in nature, yielded the proper scaling of the steady shear viscosity.

More recent work by Mead et al.,[5] Milner et al.,[9] and Graham et al.[10] have proposed theories of increasing complexity which encompass all of these behavioral modes and also additional phenomena such as contour length fluctuations. These theories can provide quantitatively accurate predictions in both the linear and nonlinear flow regime, including stress profiles, linear viscoelasticity, etc.

Despite their success, the inherent limitations of these analytic models (requirement of closure approximations, simplistic flow geometry, etc.) have led researchers to examine the fundamentals of molecular modeling and develop computer simulations of these very same entangled systems. Initial attempts via Monte Carlo methods were undertaken by Baumgärtner and Binder, where they modeled a melt as a set of freely jointed chains. They were able to demonstrate that such a system initially exhibited Rouse-like dynamics and then displayed glassy behavior as the density was raised.[11] Soon thereafter, more refined molecular dynamics based simulations by Kremer and Grest were able to clearly demonstrate the transition between Rouse dynamics for short chains and reptation for chains longer than the entanglement length. In these simulations individual chains were modeled using a bead−spring approach with a FENE-type attractive potential along with a Lennard-Jones repulsion between beads. By visualizing the configuration dynamics of polymer chains, they were able to clearly show that individual chains were confined to tubelike regions for times shorter than the disengagement time, reinforcing the idea of reptation.[12] Such MD simulations are usually limited to small system sizes and for short simulation times because this technique tracks the evolution of every atom/molecule. Thus, to simulate larger polymer systems, whose characteristic time scales can be on the order of seconds, more coarse-grained approaches (which can reproduce reptation based scalings) were pursued, e.g., the dissipative particle dynamics method.[13] Despite the success of these techniques, most do not address polymer dynamics in nonequilibrium settings, which is attracting a lot of attention due to the growing applications involving concentrated polymer solutions.[14,15] To address such situations, researchers have recently formulated various approaches. Stoltz et al. have studied the effects of flow in the transition region between the dilute−semidilute regime by simulating a number of chains in close proximity and enforcing inter- and intramolecular interactions via hydrodynamic, excluded volume, Brownian forces, etc.[16] Unfortunately, these simulations seem to be restricted to a concentrations of a few c^* due to the high computational requirements of calculating inter/intramolecular interactions. To overcome such issues, research groups have attempted more coarse-grained approaches while still capturing all the essential physics inherent in entangled polymer systems. Schieber et al. have demonstrated the use of a single chain algorithm where the effects of the neighboring chains are included in a mean-field sense, and they report remarkable comparisons between their simulations and existing experimental data.[17] Their slip-link-based approach with variable monomeric density between entanglements uses a virtual coupling mechanism between two different chains to recreate the stochastic process of constraint renewal. A potential drawback of their method is the absence of chain coupling in real space, and so one may not directly use such a scheme where dynamics are dependent on physical constraints or on absolute chain locations.

In this work, we have primarily been motivated by the newly available single molecule experimental data[18,19] which directly visualize entangled polymer behavior at equilibrium and also in shearing flows. Such data sets along with conventional rheometry allow for unequivocal evaluation of various theoretical models and simulation methods, not only in the bulk but also on the microscale level. To complement these experimental results and also better understand the microscale dynamics of polymer, we develop simulations at the entanglement level and couple the motion of different chains in *real* space. Such a method was originally proposed by Masubuchi et al.[20] for Hookean chains and by Yaoita et al. for inverse-Langevin chains.[21] Here, we incorporate a nonlinear wormlike chain force law to simulate the motion of concentrated DNA solutions and use it to examine the microscale behavior of individual chains. The inclusion of finitely extensible chains is important, especially in strong flows where polymer chains are significantly stretched and thus sample the nonlinear portion of their force−extension curve. Hookean chains, by construction, do not exhibit a maximum extension and thus fail to predict the behavior of strongly deformed polymer systems. The use of a realistic force law also motivates the usage of more sophisticated methods to solve the stochastic equations that govern the motion of a polymer system. This method can be compared with the coarse-grained method of Rakshit and Picu[22] or Padding and Briels.[23,24] Rakshit and Picu examine the motion of entangled polymer systems at equilibrium and are able to well predict end-to-end vector distributions, relaxation processes, Rouse modes, and so on. In their model, the chain ends are free to move, but the interior portions of the chain are constrained to move along a fixed path. This path remains constant until it is visited by one of the ends, at which point it is forgotten. Thus, the primitive path of a given polymer is primarily affected by its reptative motion. Padding and Briels' coarse-grained molecular dynamics method does not impose such restrictions on the dynamics of the interior path of the chains but rather views "entanglements" as points of uncrossibility where a force equilibrium holds. In addition to replicating equilibrium properties, their method has been also shown to reproduce certain nonequilibrium features such as shear stress overshoots and normal stress differences in relatively short hydrocarbon chains.[23,24] As we will see, in this work we also do not impose that an individual chain's interior move along a relatively static primitive path—our "confinement" is a result of interaction of any given chain with its neighbors which causes our primitive path to be highly dynamic and subject to the local behavior of the entangled network. Furthermore, this method is not restricted to short polymers, as many MD-based simulations are, and thus dynamics of highly entangled, long polymers can be explored.

In this paper, we first outline the general model and solution methodology. This will be followed by a description of the single

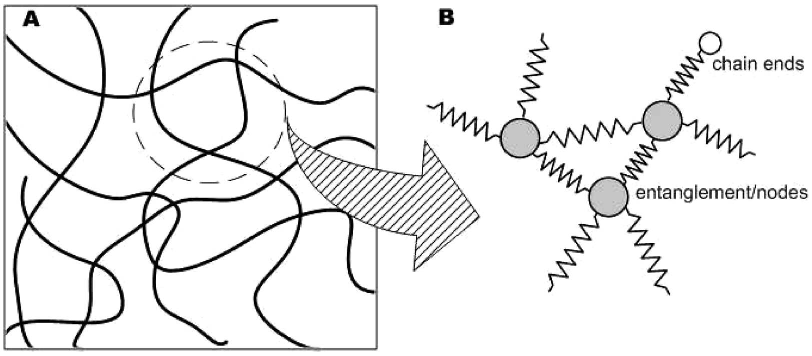

Figure 1. Discretized model (B) of an entangled polymer system (A).

molecule experiments and bulk rheology that will be used as a comparative basis for our own simulations. Next, we show the variation of the disengagement time with entanglement number and follow that with discussions about configurational fluctuations, size distributions, and the prediction of a shear stress plateau at intermediate flow strengths. The relation between microscale features and the shear stress plateau is also presented. Finally, we describe the effects of entanglement number on the linear viscoelasticity of wormlike chains.

2. Model Description

Within this model, we extend prior work[20,25] and develop a mesoscopic model for a concentrated, finitely extensible polymer system on the level of entanglements. Specifically, we model DNA molecules, which follow much stiffer force laws (discussed later in this work), and implement an implicit solution algorithm to handle strong flow conditions where an explicit framework may prove to be inappropriate. As depicted in Figure 1, each polymer chain can be thought of as a series of nodes connected by springs. Each internal node represents a point of entanglement with a neighboring chain and thus has four connecting springs. On the other hand, the end nodes simply represent the dangling ends of the polymer chains and are connected to an internal node by a single spring. Any given spring is a manifestation of a section of a polymer chain which interacts with the nodes to which it is connected via an entropically generated force that affects node motion. Such a framework is inspired by the slip-link interpretation of the tube concept within which chain dynamics near the center are restricted compared to the ends due to the presence of the nearby polymer chains. Commensurate with this simple picture, the end nodes are less restricted than the nodes in the interior because of the additional springs contributing to the motion of the latter node type.

The time evolution of this model system is a twofold process involving the motion of the nodes and the 1D motion of the monomers along the backbone of a chain, reproducing reptative motion. These dynamics are governed by spring/entropic forces, osmotic forces, flow-induced drag, and the random thermal motion of the solvent. Previous work by Masubuchi et al.[20] modeled the entropic spring forces using a Hookean force law where the force exerted by a spring is proportional to its extension. This force law is highly idealized but is widely used due to its simple form and analytic tractability. In this work, to simulate a more realistic scenario, we have elected to used the wormlike-chain (WLC) force law, shown below, which has been known to well approximate the force−extension curve of biomolecules such as DNA over a wide range of extension.[26]

$$\mathbf{F}(Q) = \frac{k_B T}{2b_k}\left(\frac{1}{(1-|Q|/Q_{max})^2} - 1 + 4\frac{|Q|}{Q_{max}}\right)\frac{\mathbf{Q}}{|Q|} \qquad (1)$$

The implementation of the WLC spring law is used within these simulations; it well approximates the force−extension behavior of biological molecules like DNA. Furthermore, it also imposes the more realistic condition of maximum extensibility upon every strand in the simulation. In comparison, Yaoita et al. simulate polystyrene molecules by using the inverse-Langevin force law (ILC) which is not as stiff as the WLC force law used here. Upon stretching, real polymers exhibit nonlinear force−extension curves which significantly deviate from their idealized Hookean counterpart, and thus one would expect predictions based on the Hookean model to become worse as stronger external deformations are imposed on any polymeric system.[27] Also, the possibility of having large extensions of entanglement strands (where explicit time integration methods poorly approximate chain dynamics) further motivates the development of an implicit simulation method to obtain more accurate predictions.

As originally accomplished for linear springs by Masubuchi et al., we develop the governing equation for the motion of a node by using a force balance around that node:

$$\frac{d\mathbf{R}^{(\nu)}}{dt} = \sqrt{\frac{N_k}{Z_0}}\frac{\sqrt{1}}{3N_c}\sum_{\alpha=1}^{N_c}\left[\frac{1}{\left(1-\frac{Q^{(\alpha,\nu)}\sqrt{n_0}}{N_k^{(\alpha,\nu)}}\right)^2} - 1 + 4\frac{Q^{(\alpha,\nu)}\sqrt{n_0}}{N_k^{(\alpha,\nu)}}\right]\frac{\mathbf{Q}^{(\alpha,\nu)}}{Q^{(\alpha,\nu)}}$$

$$+\mathbf{W}\sqrt{\frac{1}{3}} - \frac{\nabla \log \phi}{6} + Pe\kappa\cdot\mathbf{R}^{(\nu)} \qquad (2)$$

The equation has been rendered dimensionless by nondimensionalizing length with a (equilibrium distance between entanglements), time with $a^2\zeta_N(6kT)^{-1}$ (time for a node to diffuse a length a), and forces by kTa^{-1}. Z_0 is used to signify the *specified* number of entanglement strands at equilibrium and is different from the instantaneous number of entanglements experienced by a chain. As an initial approximation, the resistivity of each node is held constant during the course of the simulation. Also, the resistivity of the chain end is assumed to be $\zeta_{end} = \zeta_N/4$, which gives rise to the node-dependent coefficient preceding the spring force term.

In eq 2, $\mathbf{R}^{(\nu)}$ represents the location of node "ν". $\mathbf{Q}^{(\alpha,\nu)}$ is the vector (whose magnitude is $Q^{(\alpha,\nu)}$) representing an entanglement strand, containing $N_k^{(\alpha,\nu)}$ Kuhn segments, connecting the node "ν" to node "α". n_0 is the average number of Kuhn segments in an entanglement strand and is estimated simply as $n_0 = N_k Z_0^{-1}$.

The contributions in eq 2 are due to the nonlinear spring forces (N_c is equal to 1 or 4 for end nodes and internal nodes, respectively), Brownian forces, osmotic forces (included to prevent node clumping), and flow.[20] In our simulations in shearing flow, we specify the dimensionless rate of strain tensor as $Pe\,\kappa_{ij}$. κ_{ij} is given by $\delta_{i2}\delta_{j1}$, and the strength of the flow is controlled by the Peclet number, $Pe = \dot{\gamma}a^2\zeta_N(6kT)^{-1}$, a dimensionless ratio between the flow strength and diffusion. Finally, we model the osmotic force as the gradient of the local number density, ϕ, in the vicinity of $\mathbf{R}^{(\nu)}$.

To advance the positions of the nodes, we employ a trapezoidal scheme which requires the knowledge of the velocity of the node at the current and future time:

$$\mathbf{R}^{(\nu)}(t+\Delta t) = \mathbf{R}^{(\nu)}(t)+\frac{\Delta t}{2}\left[\frac{\mathrm{d}\mathbf{R}^{(\nu)}}{\mathrm{d}t}(t+\Delta t)+\frac{\mathrm{d}\mathbf{R}^{(\nu)}}{\mathrm{d}t}(t)\right]+O(\Delta t^2)$$

The application of this scheme results in our discretized governing equation being transformed into

$$\mathbf{R}^{(\nu)}(t+\Delta t) = \mathbf{R}^{(\nu)}(t)+\frac{\Delta t}{2}[\underline{\mathbf{F}^{(\nu,\,\mathrm{sp})}(t+\Delta t)} +\mathbf{F}^{(\nu,\,\mathrm{sp})}(t)\mathbf{F}^{(\nu,\,\mathrm{osm})}(t+\Delta t)+\mathbf{F}^{(\nu,\,\mathrm{osm})}(t)\underline{\mathbf{F}^{(\nu,\,\mathrm{hyd})}(t+\Delta t)} +\mathbf{F}^{(\nu,\,\mathrm{hyd})}(t)\mathbf{F}^{(\nu,\,\mathrm{br})}(t+\Delta t)+\mathbf{F}^{(\nu,\,\mathrm{br})}(t)] \quad (3)$$

The underlined terms depend explicitly on the *unknown future positions* of the nodes present in our system. The other terms are either known exactly or can be estimated at the current time step. The Brownian terms are generated by choosing the elements of the vector, W, from a normal distribution with $\langle W_i \rangle = 0$ and variance, $\langle W_i(t)\cdot W_i(t+\Delta t)\rangle = \Delta t^{-1}$. As an additional simplification, we assume that the osmotic forces, which vanish for a homogeneous solution, do not change appreciably over a short period of time and are thus held constant. The hydrodynamic and spring forces, at time t, are functions of the current position and thus are known. Representing all the *known* terms as $\mathbf{K}(t)$, we can now write our time advancement equation as

$$\mathbf{R}^{(\nu)}(t+\Delta t) = \mathbf{K}^{(\nu)}(t)+\frac{\Delta t}{2}[\mathbf{F}^{(\nu,\,\mathrm{sp})}(t+\Delta t)+\mathbf{F}^{(\nu,\,\mathrm{hyd})}(t+\Delta t)] \quad (4)$$

This nonlinear equation for $\mathbf{R}^{(\nu)}(t + \Delta t)$ is solved via a multidimensional Newton−Raphson procedure. Despite using a second-order trapezoidal scheme, the accuracy of this algorithm is limited to $O(\Delta t)$ because the entire system is not solved simultaneously; rather, each node is advanced holding the system fixed. This choice is made because the solution of such a coupled nonlinear system is nontrivial and computationally expensive.

As is evident from the governing equations above, hydrodynamic interactions (HI) have been neglected. It is well-known that in the concentrated regime, on length scales larger than the correlation length, perturbations in the flow field are weakened due to the high density of monomers—effectively rendering hydrodynamic interactions negligible.[3,28] Experiments on concentrated hydrocarbon chains have shown that the ratio of the screening length to the entanglement spacing varies from 0.09 in melts to about 0.15 in concentrated solutions with a volume fraction of 0.2.[29] Since we are only concerned with dynamics on the entanglement level, the small scale monomeric movements which would be affected by HI can safely be ignored. It should be noted that simulations performed in the transition region between the dilute and concentrated regimes might require the inclusion of HI to faithfully represent experiments.[16]

To start our simulations, the ends of N_c polymer chains are randomly placed in a cubical box of side length, L_{cell}. The length is chosen to impose a density ($N_c Z_0 L_{\mathrm{cell}}^{-3}$) of 10 entanglement strands in a volume of a^3. To initialize the network, each chain is then entangled with other chains present nearby, and subsequently, this system is allowed to thermally equilibrate under no-flow conditions. During this equilibration period, additional nodes were created as outlined previously. Figure 2 is representative of our system just after these initialization steps have been completed. During typical runs, between 256 and 512 chains are simulated and the time step is varied between 0.01 for low flow conditions and 0.001 for fast flows. Most of our simulations were run with Z_0 ranging from 7 to 15, and we chose to use 700 Kuhn steps per chain which is close to the length of T4-DNA, used by Jary et al.[30] As mentioned previously, we use a Pade approximation to the wormlike-chain force law[26] for the node interconnects throughout this work.

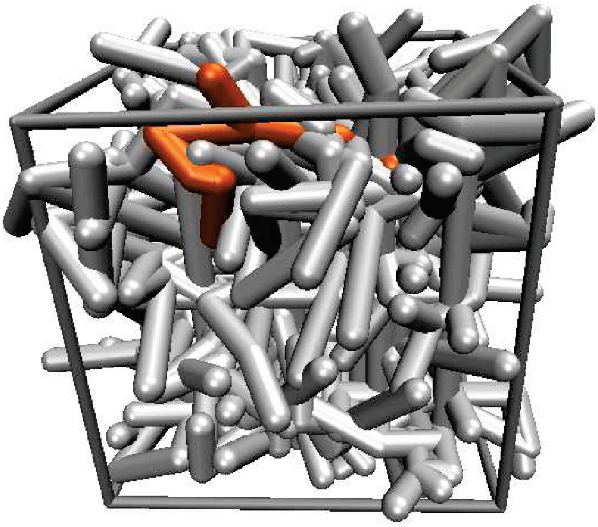

Figure 2. A snapshot from our simulation of an entangled polymer system, with $Z_0 = 10$, in a unit cell. The unit cell boundaries are shown along with one polymer chain highlighted in orange.

In addition to the movement of nodes, reallocation of monomers between the entanglement strands along the backbone of any given chain must occur to account for the reptative behavior in entangled systems. As in the case for node dynamics, we can use a force balance around a chain's internal node and write the equation for the flux of monomers from spring v to $v + 1$ as

$$\dot{n} = \frac{N}{3Z_0}(|\mathbf{F}^{(\nu+1,\,\mathrm{sp})}|-|\mathbf{F}^{(\nu,\,\mathrm{sp})}|)+2\frac{N}{Z_0}\sqrt{\frac{1}{6}}w \quad (5)$$

To derive eq 5, we have assumed a constant monomeric density of $N(Z_0)^{-1}$ over the backbone of a chain and have implemented a 1D Wiener process using a stochastic scalar variable, w, to include the effects of thermal motion. This monomer reallocation has been used in other models and is essential in Brownian dynamics simulations of entangled polymers.[20,31] Because of the $O(\Delta t)$ accuracy of the node dynamics, we elect to use a simple Euler integration scheme for monomer reallocation. However, we also impose a lower bound (we use three Kuhn steps) on the number of Kuhn steps that can exist in any given entanglement strand. It has been shown that dynamics are insensitive to this lower bound as long as it is less than the equilibrium value for Kuhn steps per entanglement strand.[20]

Just as important as the motion of the nodes and monomers is the dynamic process of creation and destruction of entanglement nodes. This dynamic process distinguishes a concentrated polymer system from a cross-linked network where nodes represent fixed time-invariant links between chains. Nodes are created/destroyed during the course of a simulation based on the number of monomers at a chain end as proposed by Masubuchi et al.:

$$\frac{1}{2}\left(\frac{Z}{Z_0}\right)^4 < \frac{n}{n_0} < 1+\frac{1}{2}\left(\frac{Z}{Z_0}\right)^4 \quad (6)$$

Equation 6 is based on the rule that an entanglement node should be destroyed if the number of monomers becomes low and

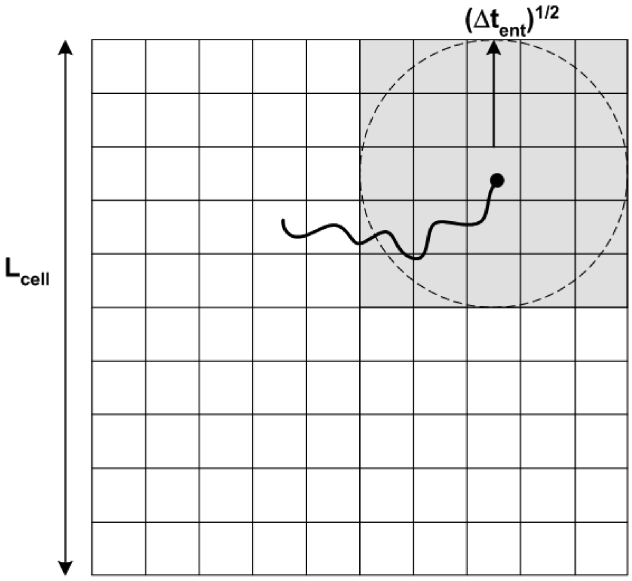

Figure 3. Cell list method. Partners for the chain shown are only sought for within the shaded region. By tracking the locations of the polymer chains in the simulation, we can efficiently enforce the entanglement creation process.

conversely if the number of monomers becomes high; then it would be a candidate to get entangled with another neighboring chain. Therefore, in our simulations, if the number of monomers in the end segments falls below half the equilibrium value, then entanglement nodes are destroyed, and if the number increases above 1.5 times the equilibrium value, then a new entanglement node is be created (Figure 4). The form of eq 6 has been chosen to force the number of entanglements to remain near the prescribed equilibrium value.[20] A check of this criterion is made after every Δt_{ent} time units, and a suitable partner is sought in the region near the chain end via a cell list. The cell list method is illustrated in Figure 3. During our simulations, we divide the simulation cell into cubical boxes, each with a volume equal to $L_{\text{cell}}^3/1000$, and track the strands present in any given box. Using this information, when we want to create an entanglement at a particular chain end, present in a given box, we can simply search for suitable partners in adjacent boxes instead of the entire simulation cell. The number of cells searched, N_s, is chosen such that the area searched contains a sphere of radius $(\Delta t_{\text{ent}})^{1/2}$. Under this convention, the minimum number of boxes searched is limited to unity, and no entanglements are created if a suitable partner is not found. It must also be noted that the size of each cubical box increases with increasing number of chains and Z_0. However, for the typical parameters used in this work, the length of each side of the box maintained to be less than the equilibrium entanglement spacing, a.

If a suitable partner is found within the search region, then an entanglement node is created without violating the maximum extensibility and while also conserving the number of Kuhn steps per chain. The time between entanglement checks is important because it essentially controls the amount of constraint release events that we allow the system to undertake. At this stage, we envision two reasonable ways in which one can set Δt_{ent}. First, one might set Δt_{ent} for a certain chain end to be equal to the amount of time elapsed since the last time it created an entanglement. Thus, whenever we attempt to find partners for the chain end, we search progressively larger volumes in accordance with the fact that the chain end is able to explore a greater amount of space as time progresses. Alternatively, one might simply set Δt_{ent} to be some fraction of the Rouse time of the chain end and search the corresponding volume [of size $(\Delta t_{\text{ent}})^{1/2}$] every Δt_{ent} time units.

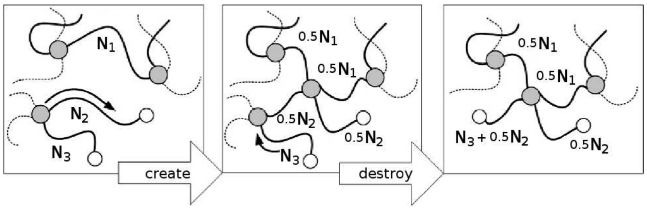

Figure 4. Example of a chain experiencing the creation and the destruction of a node. First the strand with N_2 monomers at the end reptates and entangles with a neighboring chain. The existing numbers of Kuhn steps are reallocated among the new entanglements. Next, reptation causes the number of Kuhn steps in a different portion of the chain, N_3, to drop, leading to the destruction of a node while conserving Kuhn step number.

For most of our simulations, we have chosen the latter method for simplicity (a discussion about the choice of this time scale on observed properties is presented later in this article, in sections 3.6 and 4). For low to moderate flow rates, $\Delta t_{\text{ent}} = 0.1$ seemed to be acceptable (evidenced by the lack of a physical predictions); however, this value is lowered for stronger flows and larger entanglement numbers. Despite the importance of the frequency of constraint release, we believe that the details of the entanglement creation/destruction process (e.g., exact locations of the entanglements being created) are not important since the local conformations relax over a time scale much smaller than any time scale of interest. This dynamic process causes the number of entanglements experienced by chains to be a stochastic quantity, and it should be noted that we are directly using the microscale structure of the system to recreate constraint release events. We do not use additional parameters to model this phenomenon, as is the case when modeling constraint release as a diffusion process requiring the input/calculation of a characteristic time scale.[10,31]

Such an algorithm will work only if any given polymer chain is able to find a suitable partner whenever required by eq 6. Thus, we require spatial homogeneity to ensure that any polymer chain be provided with a sufficient number of potential entanglement partners, irrespective of its position. This problem is overcome in our boundary-less simulations by using periodic boundary conditions, which allows one to simulate an infinite medium using only a finite number of polymer chains. Under conditions of shear, we use the Lees–Edwards boundary conditions (LEPBCs) which replicates the state of a *unit cell*, centered around the origin, over the entire 3D space. For a system with an ambient shear flow field given by $U_i = \dot{\gamma} x_j \delta_{i1} \delta_{j2}$ a node present at $\langle x, y, z \rangle$ has images at $\langle x, y, z \rangle + L\langle \dot{\gamma} t n_y + n_x, n_y, n_z \rangle$, where L is the size of the cubic unit cell and $\{n_x, n_y, n_z\}$ are integers.[32] So by using LEBPCs, we can make sure that even the polymer chains near the edges of a central unit cell are surrounded by a well-entangled polymer network composed of other chains or their images.

3. Results and Discussion

3.1. Experimental Data. Our primary motivation is to develop an efficient simulation method that can be used to gain insight into the microscale dynamics of entangled polymer solutions. A hurdle facing any such development is the availability of experimental data with which results can be calibrated and compared. Over the past few decades, experimental investigations into the behavior of concentrated polymer solutions have yielded a vast amount of bulk rheological data for a variety of systems—both synthetic[33,34] and natural[35,36]—in a variety of architectures,[37,38] blends,[39] etc. Despite providing insights into the macroscale characteristics of entangled systems, a direct measure of the molecular response of these same systems has remained largely unknown, until recently. The advent of single molecule techniques has thus resulted in the direct visualization of DNA molecules at the molecular level,[18] which allow us to probe the microscale motion of entangled polymers with great precision. The comparison of simulation results with both bulk and molecule-level data is essential in assessing the validity of the simulation model and evaluating the limits of the numerical procedure.

In this work, in addition to certain theoretical results, we attempt to compare and contrast our microscale results with experimental single molecule findings obtained previously by Teixeira et al. They demonstrated the ability to create homogeneous concentrated solutions of individually stained molecules of double-stranded λ-DNA with concentrations varying from approximately $10c^*$ to $30c^*$, with the highest concentration corresponding to about 17 entanglements per chain.[19,40] These polymer solutions were exposed to a series of bulk rheological tests, and classic signatures of concentrated solutions such as a plateau in the shear stress were observed.[19]

More importantly, these same solutions were then exposed to shearing flows of varying strengths, and the motions of individual molecules were recorded. This enabled the acquisition of both static and dynamic metrics to better understand concentrated polymer dynamics from a *single molecule* perspective. The shear flows imposed during their single molecule studies were carefully quantified using particle tracking to verify the absence of concentration-based instabilities that have recently been reported in entangled polymer systems by Boukany et al.[41] These reported instabilities were for DNA solutions but were much more entangled than those used in Teixeira et al.'s single molecule experiments. Actually, permanent shear banding was found for only highly entangled systems (entanglements per chain of 60 and 156), and in contrast only relatively weak flow in homogeneities were reported for solutions corresponding to 24 entanglements per chain, a value that is comparable to the solutions used by Teixeira et al. Nevertheless, Teixeira et al.'s particle tracking characterizations also resulted in flow fields, shown in Figure 5, that were linear for the entire range of flow rates explored. Teixeira et al. acknowledged the existence of wall slip and observed the extent of this slip layer to increase with concentration and diminish with flow strength. Their particle tracking measurements verified the existence of nearly constant shear rates (away from the slip layer) across the channel, assuring the absence of any gross spatial instabilities. The existence of both bulk and single molecule data in the absence of flow nonidealities provides us a unique set of data and prompted its use as a basis with which to evaluate our own results.

For bulk rheological measurements, we turned to the experimental findings of Jary et al.,[35] who have performed rheological measurements of longer T4-DNA strands, the parameters of which resemble those used in the simulations presented in this paper. Their rheological results will be used to examine the accuracy of our predicted changes in shear stress as a function of shear rate.

3.2. Time Scale Scaling. As an initial test of our simulation procedure, we analyzed the correlation relaxation of the end-to-end vector, $\mathbf{P}(t)$. Doi and Edwards, using reptation theory, initially proposed that the correlation function $\Phi(t) = \langle \mathbf{P}(0)\cdot\mathbf{P}(t)\rangle$ was governed by the disengagement time—so-called because it was also the time scale over which a chain reptates out of its original tube and renews its configuration. The disengagement time was predicted to vary as the length of the polymer chain to the third power and is commonly written in terms of the Kuhn length, b_k, number of Kuhn steps, N_k, the friction coefficient of a Kuhn segment, ζ_k, and the equilibrium entanglement spacing, a, as[3]

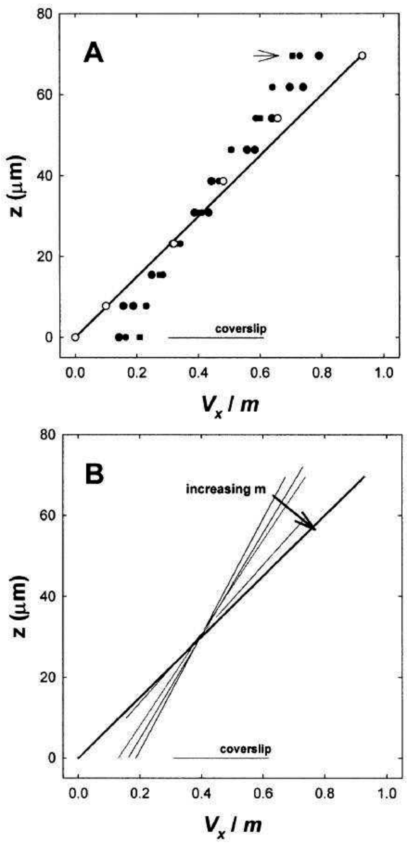

Figure 5. Experimentally observed velocity profiles in concentrated DNA solutions ($16c^*$), along with corresponding linear fits.[40]

$$\tau_D^{(t)} = \frac{N_k{}^3 b_k{}^4 \zeta_k}{\pi^2 k_B T a^2} \qquad (7)$$

We use the notation $\tau_D^{(t)}$ to refer to the theoretical prediction of the disengagement time to differentiate it from its measured value, $\tau_D^{(m)}$, obtained via simulations. The corresponding Rouse times are obtained by dividing the disengagement times by $3Z_0$.

To obtain a suitable estimate of the disengagement time from our simulations, we directly record $\mathbf{P}^{(n)}(t)$, the end-to-end vector of chain n at time t, and subsequently extract the correlation function as

$$\Phi(t) = \frac{1}{N}\sum_{n=1}^{N}\left[\frac{1}{T-k+1}\sum_{k=1}^{T-t}\mathbf{P}^{(n)}(k+t)\cdot\mathbf{P}^{(n)}(k)\right] \qquad (8)$$

In addition to ensemble averaging, eq 8 represents a time average (at equilibrium) over all chains as well—this time average helps smooth the correlation function by effectively increasing the points that contribute to the average at any t. Subsequently, the longest relaxation time—disengagement time—was extracted by measuring the slope of the linear portion of the curve of $\Phi(t)$ vs t on a log−linear plot, and in Figure 6, we have plotted this characteristic time as a function of the number of entanglement strands in a chain. As is seen in Figure 6, we find $\tau_D^{(m)} \sim Z^{3.4}$, which is slightly different from the classical tube theory prediction of $\tau_D^{(t)} \sim Z^3$. These scalings in the longest relaxation time are clearly different from those in the dilute case (where the

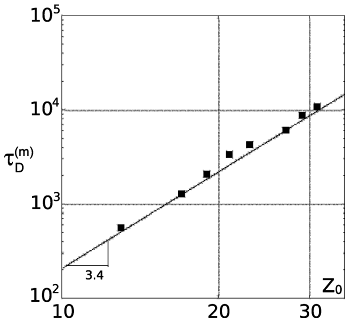

Figure 6. Scaling of the measured orientational decay time scale with imposed number of entanglement strands.

longest relaxation time varies as the square of the length, in the absence of hydrodynamic interactions).

This scaling had been observed in many experimental cases and has previously been the focus of debate as to whether the exponent of 3.4 was an aberration arising due to experimental limitations or a sign of conceptual shortcomings.[3,42] Theoretical developments addressed this issue and modern theories that include physical effects such as contour length fluctuations (CLF) do predict an exponent of 3.3−3.4.[43] Length fluctuations increase the rate at which chain ends sample the local environment and thus enhance the rate at which orientations decay. Thus, in short to moderate length chains, $Z_0 \leq 100$, where end effects play a significant part in the overall chain dynamics, CLF manifest themselves as a stronger dependence of the relaxation time scale on length. As a natural extension, it has been conjectured that for very long chains the scaling exponent reverts back to a value of three, due to the diminished effect of end dynamics. This conjecture has been demonstrated independently by Doi and Milner et al.[42,43]

On the basis of this understanding, it seems that our simulations are able to capture the effect of entanglements on the longest relaxation time, which is expected when a model is able to properly reproduce reptation. However, more importantly, our model also seems to capture the corrections arising due to contour length fluctuations, at low entanglement numbers, evidenced by our measured scaling exponent of 3.4. To examine the effects of Δt_{ent}, we ran simulations for $Z_0 = 10$ and compared the relaxation times predicted when Δt_{ent} was set to be either $5\Delta t$ or $10\Delta t$. We found that both values of Δt_{ent} differed by ~4% only, suggesting that the dynamics near equilibrium are not significantly affected by the choice of Δt_{ent}. This supports the idea that constraint release does not play a dominant role under near-equilibrium conditions and that, from a simulation stand point, topological changes occur on time scales longer than the values of Δt_{ent} examined here.

3.3. Time Traces. Using our simulations, we were able to track the evolution of the configuration of individual polymer chains. Specifically, we studied the time traces of the components of the end-to-end vector, $\{P_x(t), P_y(t), P_z(t)\}$, and the angle made with the direction of flow, defined as $\theta(t) = \tan^{-1}(P_y/P_x)$.

For systems with $Z_0 = 15$ at low flows, $\dot{\gamma}\tau_D^{(t)} = 0.2$, we see in Figure 7 a typical time trace for a polymer in our entangled simulation. We see a wide but relatively smooth variation in the angle, which spans all possible values from $-\pi$ to π. Also, we observe fluctuations in not only the flow and gradient directions but also the neutral direction as well. The magnitudes of these fluctuations are approximately equal in all directions, which is expected due to the inability of the flow to deform the polymer away from its equilibrated state. It is interesting to note that the observed fluctuations can be long-lived and persist for multiple disengagement times.

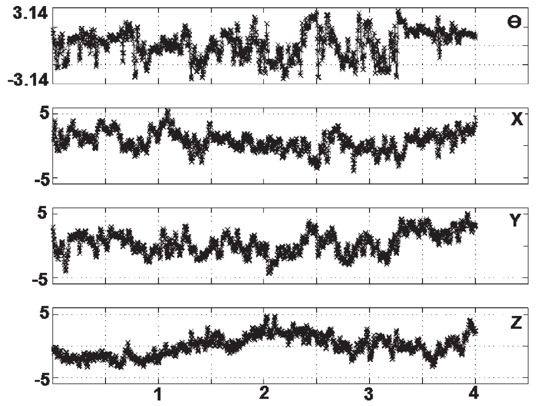

Figure 7. Time traces of the angle and projections of the end-to-end vector for $Z_0 = 15$ at $\dot{\gamma}\tau_D^{(t)} = 0.2$. Quantities are dimensionless, and the time axis is normalized by the disengagement time.

Moving to stronger flow rates, we observe more interesting dynamics for $\dot{\gamma}\tau_D^{(t)} = 22.4$, where the flow is strong enough to significantly perturb the conformations of individual molecules. Under these conditions, polymer chains would be expected to be more stretched and exhibit larger fluctuations than in the slow flow scenarios. To demonstrate the variety of conformational dynamics, we present Figures 8 and 9 which depict individual molecules as they undergo stretching and tumbling motion in shear. In Figure 8, we see polymer molecules display fluctuations on the order of 10−20 times the equilibrium entanglement spacing (all lengths are nondimensionalized by the equilibrium entanglement spacing) in the flow and vorticity directions and approximately half that in the neutral direction. Since the maximum length of our polymer chains is 102, these time traces show excursions that are 20% of this maximum value.

In addition to chain stretching, we also see time traces that depict "tumbling" behavior, analogous to that observed previously for dilute DNA solutions.[44] In Figure 9, for example we start at a time of 7.4 with the polymer being aligned opposite to flow direction. This is followed by a slow "half tumble" where the angle transitions to zero, presumably due to the "back" of the molecule diffusing upward in the gradient direction and then getting convected past the "front" end. During this process the size in the flow direction changes sign and becomes increasingly positive while the "y" projection remains reasonably constant. Then the molecule temporarily remains aligned and stretches in the flow direction (between times of 7.6 and 7.8). Finally, we notice a rapid change in the angle to $-\pi$ accompanied by the projections in the flow and gradient directions becoming negative, signifying the completion of this tumbling event. This tumble occurs over the course of one disengagement time and is thus different from the rapid tumbling observed in dilute solutions.[44] Such tumbling phenomena have also been observed in molecular dynamic simulations of long hydrocarbon chains, performed by Kim et al. Most of the results in that study were obtained in strong flows (i.e., flows faster than the associated Rouse time scale), and the tumbles occurred on a time scale much shorter than the Rouse time. Nevertheless, these rotational fluctuations were seen to affect chain statistics such as chain size and orientation and thus in turn are expected to affect the rheological properties of the solution itself.[45] In our simulations we see similar fluctuations, albeit not as frequently, which involve a concerted change in the sizes of flow and gradient direction. Because of the differences

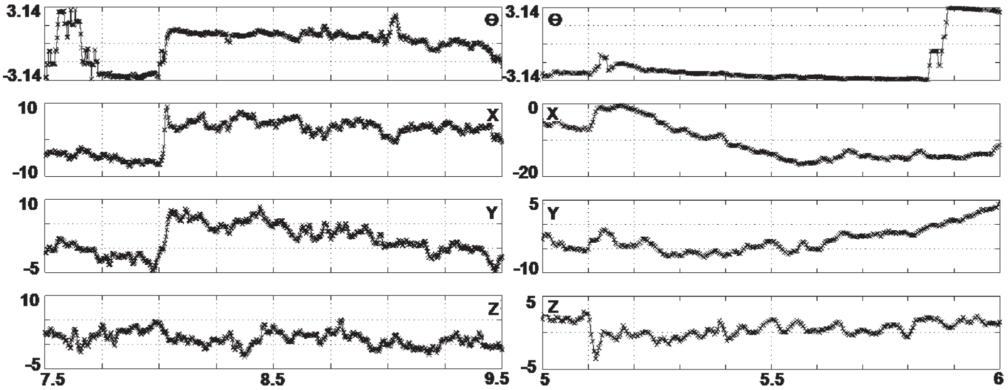

Figure 8. Time traces showing significant stretching in the flow-gradient plane for $Z_0 = 15$ at $\dot{\gamma}\tau_D^{(t)} = 22.4$. Quantities are dimensionless, and the time axis is normalized by the disengagement time.

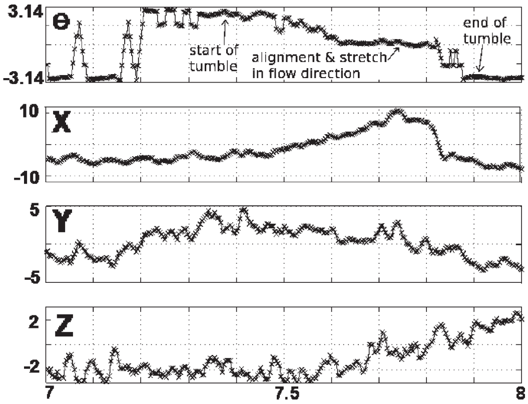

Figure 9. Time traces of the angle and projections of the end-to-end vector for $Z_0 = 15$ at $\dot{\gamma}\tau_D^{(t)} = 22.4$. Quantities are dimensionless, and the time axis is normalized by the disengagement time.

in chain length and density, the rotational dynamics in our simulations seem to be hindered and cause tumbling to occur over a period of time comparable to the disengagement time of the polymer molecules. During such long tumbles, other restretching/retraction events are expected to occur, thus diminishing the frequency of complete tumbles in our simulations. An increased rate of shear enhances, these rotational fluctuations and decreases the time between tumbling events.

3.4. Power Spectral Density. Another dynamic quantity that we were able to extract is the power spectral density (PSD) of polymer extension in the flow direction. The PSD of a time-dependent signal refers to its frequency content, more specifically the distribution of the power among the various frequencies. It can be used to examine the relative contributions of various frequencies to the overall behavior of stochastic time-dependent processes and identify important frequencies in a spectrum, e.g., frequencies at which a process tends to repeat itself. It has been demonstrated that for a stationary process, $x(t)$, the PSD can be calculated simply as the Fourier transform of its autocorrelation function, $R(t) = \langle x(\lambda)\, x(\lambda + t)\rangle$.

$$S(\omega) = \mathscr{F}(R) = \int_{-\infty}^{\infty} R(t) \mathrm{e}^{2\pi i \omega t}\, \mathrm{d}t \qquad (9)$$

For our purposes, we will be analyzing the power spectra of the end-to-end vector projected into the flow direction using a periodogram which estimates the PSD for discrete time-dependent sequences.[46] For concentrated systems at equilibrium, the correlation function for the end-to-end vector is expressed using reptation theory as[3]

$$\langle \mathbf{P}(0)\, \mathbf{P}(t)\rangle = N_k {b_k}^2 \sum_{p \in \{1,3,5,\ldots\}} \frac{8}{p^2 \pi^2} \mathrm{e}^{-p^2 t/\tau_D^{(t)}} \qquad (10)$$

Such a form for the correlation is identical, albeit with a different time constant, to that obtained for dilute polymer systems. Studies of the spectral content of polymer motion in the dilute regime have been previously undertaken by Hur et al., where they were able to study the effect of flow and discretization on the power spectrum of the end-to-end vector. They demonstrated both analytically and through Brownian dynamic simulations that at equilibrium the power dependence on frequency changed from $S(\omega) \sim \omega^{-2}$ to $S(\omega) \sim \omega^{-1.6}$ upon the addition of higher internal modes and that the spectrum exhibited regions of varying slopes upon the imposition of a shearing flow.[47]

For our concentrated system, under equilibrium conditions, we find that $S(\omega) \sim \omega^{-m}$ with m varying between 1.4 and 1.6 for Z_0 between 10 and 15 and $\omega\tau_D^{(t)} > 1$, the same behavior as for dilute solutions. Such correspondence is not entirely unexpected given the similarities between the dynamics of the end-to-end vectors and also in light of the fact that the presence of entanglements plays the role of adding higher order modes (which is the primary cause of the exponent being -1.6 in the dilute case).

To capture flow-induced changes, we performed nonequilibrium simulations for chains with $Z_0 = 10$ for a range of flow rates, $\dot{\gamma}\tau_R^{(t)} \in [0.003-3.04]$. Conventional understanding suggests that these flow rates represent drastically different scenarios: $\gamma\tau_R^{(t)} < 0.033$ being the weak flow regime, $0.033 < \dot{\gamma}\tau_R^{(t)} < 1$ corresponding to the so-called plateau regime, and $\dot{\gamma}\tau_R^{(t)} > 1$ representing strong flows where chain stretching is induced. In contrast to dilute solutions,[47] the shape of the PSD is relatively featureless and does not contain an intermediate region with a high slope, which arises due to the coupling of flow effects and Brownian fluctuations. However, our simulations reveal that as the flow strength is increased, the PSDs start to decay with a higher exponent, indicating relatively diminishing contributions from the high-frequency region. We observe that for $\dot{\gamma}\tau_R^{(t)} = 0.003$ the PSD decays as $\omega^{-1.6}$ and at 3.04 the scaling changes to ω^{-2}. Single molecule fluorescence microscopy was used by Teixeira et al. to measure these dynamic PSDs for λ-DNA,[19] and they also report a smooth transition of the decay exponent from approximately -1.4 to -2 in a range of flow rates that extended from the low flow all the way to the stretching regime.[48]

The limiting decay exponent of -2 in the fast flow regime is the same as the decay exponent for dumbbells at equilibrium.

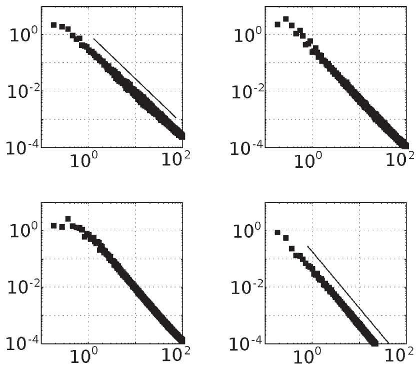

Figure 10. Dynamic power spectral densities for $Z_0 = 10$, for (clockwise from top left) $\dot{\gamma}\tau_R^{(t)} = 0.003$, 0.10, 1.01, and 3.04. Dimensionless frequencies $\omega\tau_D$ are plotted on the x-axis, and the power is on the y-axis. The power has been normalized such that the power at zero frequency is equal to unity. The lines in the top left and bottom right have slopes of -1.55 and -2, respectively.

This resemblance might indicate that as in the case of the equilibrium dumbbell the dynamics of highly stretched concentrated polymers is dominated by a small number of low-frequency modes. This in turn could possibly be caused by the ability of the flow to stretch polymer chains with greater efficiency as the shear rate is increased beyond $\dot{\gamma}\tau_R^{(t)} > 1$, and as increased stretching is encountered, the higher modes with shorter relaxation times are attenuated. In both dilute and concentrated cases, if the correlation function is well approximated as a single-exponential decay, then the corresponding power spectrum would simply scale as $S(\omega) \sim \omega^{-2}$ for frequencies in excess of the inverse characteristic time. This result is evident in both single molecule experiments and within our simulation framework.

3.5. Size Distributions. Until very recently, the configurations of polymer chains in entangled polymer solutions have been analyzed via indirect methods such as light scattering and birefringence—methods which probe the *average* sizes of the polymer molecules. However, single molecule techniques, which have been used to provide direct evidence of molecular scale phenomena such as coil–stretch transitions and conformational hysteresis, have been successfully modified to provide visual evidence of entangled dynamics in concentrated λ-DNA solutions.[18,49]

Our simulations provide a convenient method to analyze and understand configuration changes that are brought upon by various forces acting on a concentrated polymer system. As before, flow-induced effects were examined by subjecting a well-entangled polymer system composed of wormlike chains to shear flow, recording chain configurations, $\mathbf{r}^{(n)}$, and calculating the molecular sizes as defined by

$$X_i^{(n)} = \max\{r_i^{(n)}(t)\} - \min\{r_i^{(n)}(t)\}$$

$$\langle X_i \rangle = N^{-1} \sum_{n=1}^{N} X_i^{(n)} \qquad (11)$$

This measure of chain size was chosen instead of the previously used end-to-end measure to be compatible with measurements obtained via experiments, which cannot easily locate chain ends. Our results for $Z_0 = 7$, 10 are shown in Figures 11 and 12, respectively. These histograms were generated by measuring the chain sizes in the flow direction, normalizing by the maximum length $[(Z_0 N_k)^{1/2}]$ and then binning the distribution in bins of width 0.01.

We see that the distribution of chain sizes is not peaked even at moderate flow strengths and is very broad for strong

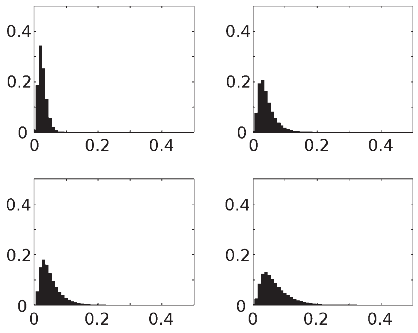

Figure 11. Distribution of chain sizes in the direction of flow normalized by maximum length $Z_0 = 7$ (clockwise from top left: $\dot{\gamma}\tau_R^{(t)} = 0.028$, 1.44, 2.18, and 4.34).

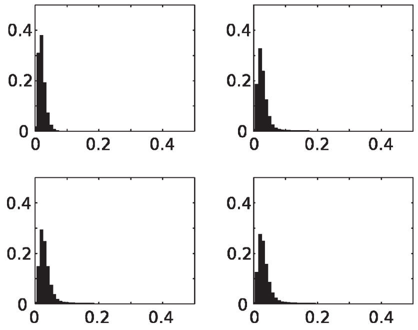

Figure 12. Distribution of chain sizes in the direction of flow normalized by maximum length $Z_0 = 10$ (clockwise from top left: $\dot{\gamma}\tau_R^{(t)} = 0.02$, 1.52, 3.04, and 4.06).

flows, i.e., $\dot{\gamma}\tau_R^{(t)} > 1$, implying the presence of a large range of conformations that deviate significantly from the "mean" conformation. For low entanglement numbers, the average extension varied from 3.1% of maximum length at the lowest flow rate to 7.3% at the highest rate of shear. The corresponding values for $Z_0 = 10$ were 2.69% and 3.8%. Despite these low values for the averages, in both cases we find broad distributions of polymer size and observe the presence of highly stretched conformations. For $Z_0 = 10$ the maximum observed extension is greater than 40% and in excess of 51% for $Z_0 = 7$. Thus, in both cases the nonlinear region of the force–extension curve is sampled upon the onset of chain stretch. The previously mentioned work of Kim et al. using MD simulations also contained wide distributions of extension in stretching flows. Furthermore, Teixeira et al.'s work with λ-DNA systems revealed wide distributions in extension with the maximum stretch exceeding 42% at flow strengths equal to 5.4 (relative to the fast relaxation time measured via single molecule experiments) at a polymer concentration of $35c^*$. Similar extensions were observed in λ-DNA systems with concentrations of $23c^*$ and $10c^*$. However, the average extension observed in these single molecule experiments was ~20%, which is significantly larger than the value that we observe via our simulations. Once again, the differences in chain size and monomer distribution between entanglements strands might affect these average values. A lower number of Kuhn steps in an entanglement strand (i.e., higher number of entanglements) would result in the springs being stiffer and would be better suited to resisting the stretching tendencies due to the ambient flow, resulting in lower average stretch. Despite these differences, the presence of large tails in size distributions raises questions regarding the validity of the commonly invoked preaveraging assumption. The preaveraging assumptions is known to work best when the polymer molecules in the systems are closely clustered about their

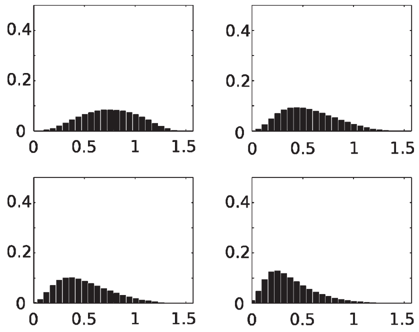

Figure 13. Distribution of angles at various flow strengths for $Z_0 = 7$. Shear rates are the same as those in Figure 11.

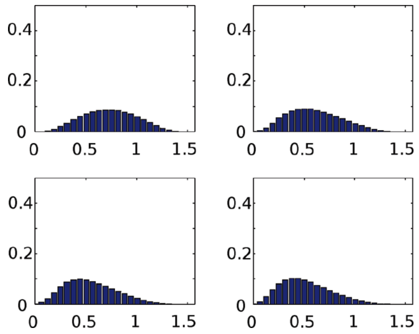

Figure 14. Distribution of angles at various flow strengths for $Z_0 = 10$. Shear rates are the same as those in Figure 12.

mean, thus validating the usage of a single *average* value. However, this assumption breaks down relatively quickly when shear flow induces a wide distribution of chain extension and renders the tails non-negligible.

To further explore this conformational variation, the orientational dispersion exhibited by our polymer system was examined. We measured the distributions of the angle corresponding to the size of the chain, projected into the flow-gradient plane, as given by

$$\theta^{(n)} = \tan^{-1}\left(\frac{X_y^{(n)}}{X_x^{(n)}}\right) \tag{12}$$

As defined above, $\theta = 0$ corresponds to chains that are nearly aligned with the flow direction and $\theta = \pi/2$ represents chains that are aligned in the flow-gradient direction. The measured angle distributions (Figures 13 and 14) show the change in the distributions of the angle as a function of flow strength. We notice that at near equilibrium, for all cases, the distribution of sizes is symmetric around $\pi/4$, as expected, and remains so until $\dot{\gamma}\tau_R^{(t)} \sim O(1)$, when the PDF becomes skewed to the left indicating the increased alignment of the chains in the system. In addition, we observe that at a given relative flow strength the PDF becomes more skewed with *decreasing* number of entanglements. However, it is important to note that even at very high flow strengths it seems that polymer chains maintain a finite angle with the flow direction, and complete alignment is never observed. Such polymer conformational dynamics correspond to the observed plateau of the orientation angle $\dot{\gamma}\tau_R^{(t)} < \dot{\gamma} < \dot{\gamma}\tau_R^{(t)-1}$, obtained via birefringence experiments of entangled polystyrene solutions.[34] This "frozen" orientation angle has been described previously (without direct evidence) to be primarily caused by constraint release events. CR affects both the orientation of the polymer and also the number of Kuhn steps within an entanglement strand, thus in essence influencing the drag and entropic forces felt by entangled chains. A theoretical analysis of these effects has shown that a balance between the entropic elastic forces and the drag forces can lead to the observed plateau in orientation.[50] These effects of constraint release also manifest themselves in bulk properties such as shear stress, which will be addressed later. Our simulations provide the first direct evidence of this phenomenon.

This behavior reinforces the notion that in many concentrated polymer systems chain properties are not described by a single system defined mean value and actually possess broad distributions of chain stretch and orientation. McLeish[55] also discusses the presence of these broad size distributions based on primitive-tube simulations but conjectures that the pre-averaging assumption might be justified for systems with a large number of entanglements. This justification is based on the idea that since the orientational distribution is sampled by tube segments, chains with higher number of entanglements (tube segments) are able to better sample the overall distribution, and thus their configuration would be clustered around some system defined mean value. However, on the basis of our simulations, we see that this condition is not met for entanglement numbers up to 10−15 and that stretch, and orientational distributions exhibit large tails for a wide variety of flow conditions.

3.6. Shear Stress. One of the signatures of an entangled solution is the appearance of a stress plateau under conditions of shear. This plateau emerges for a wide range of flow rates, roughly corresponding to $\tau_D^{-1} \leq \dot{\gamma} \leq \tau_R^{-1}$. Since $\tau_D/\tau_R = 3Z_0$, the extent of this plateau increases with molecular weight and can persist over multiple decades of $\dot{\gamma}$. Coincidentally, the emergence of the shear stress plateau highlighted the shortcomings of the original reptation model which actually predicted a sharp decrease in shear stress, ($\sigma_{12} \sim \dot{\gamma}^{-1/2}$) for flow rates in excess of the inverse disengagement time.[5]

Physically, the shear maximum predicted by the reptation model was attributed to the excessive alignment of chains at flow rates in excess of the inverse disengagement time. The problem was further exacerbated by the assumption of constant tube length which also limited the extent to which chains were able to stretch. However, simply including chain stretch did not remove the stress maximum but relegated it to a higher strain rate. Chain stretch by itself cannot remove the stress maximum because of the separation of relative time scales of chain orientation and chain stretch. The former is controlled by the disengagement time, and the latter is induced by high shear rates relative to the Rouse time scale. Since these time scales are separated by a factor of the number of entanglements, chain stretch is unable to modify the stress behavior at $\dot{\gamma} \sim \tau_D^{-1}$—exactly where the shear maxima occurs.

However, the inclusion of constraint release mechanism was demonstrated, somewhat counterintuitively, to alleviate the onset of shear thinning.[51] These constraint release events, as demonstrated above, prevent the complete alignment of chains in the flow direction and thus help maintain a greater amount of stress than previously predicted by the reptation theory alone.[5,50] Furthermore, convection-induced constraint release becomes dominant at shear rates greater than the inverse of the disengagement time and thus is active at the onset of the stress plateau and prevents the aphysical drop in shear stress.

The model described in this paper inherently contains all these modes of polymer motion. The chains are allowed to stretch in response to flow-induced deformations and account for end-fluctuations by varying the friction of the ends relative to the internal segments of a chain. To incorporate the effects

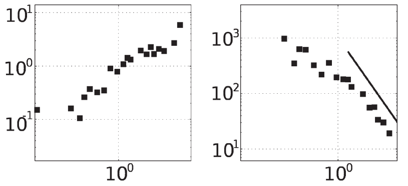

Figure 15. Left shear stress (σ_{12}) and viscosity versus ($\sigma_{12}\dot{\gamma}^{-1}$) vs shear rate ($\dot{\gamma}\tau_{\mathrm{D}}^{(\mathrm{m})}$) for $Z_0 = 10$. The solid line has a slope of −0.97.

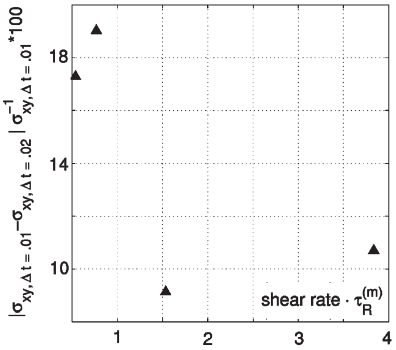

Figure 16. Percent error in the measured steady shear stress for $Z_0 = 10$, between simulations performed at $\Delta t = \Delta t_{\mathrm{ent}} = 0.01$ and $\Delta t = \Delta t_{\mathrm{ent}} = 0.02$.

of flow, other numerical methods have used ad-hoc models[4] or have used a consistent tuning procedure to obtain characteristic parameters.[31] In this work, there are no adjustable parameters used for the inclusion of constrain release events, which are driven purely by the motion of the chains constituting an entanglement. Thus, any flow-induced changes in the motion of any given polymer directly affect the lifetime of any given constraint, effectively coupling the two phenomena.

To examine the performance of this model in shear, we ran multiple simulations for chains with 700 Kuhn steps, varied the imposed number of entanglements per chain, and extracted the shear stress (σ_{12}) vs flow rate curve. The shear stress is calculated using the spring forces as $\langle F_1^{(\mathrm{sp},\alpha)} Q_2^{(\alpha)} \rangle_\alpha$, where the ensemble consists of all the entanglement strands in the simulation. The stress data for $Z_0 = 10$ are presented in Figure 15, along with the corresponding shear viscosity curve ($\eta(\dot{\gamma}) = \sigma_{12}\dot{\gamma}^{-1}$).

As can be seen, the shear stress data show the emergence of a plateau, and we see a shear thinning exponent of nearly −1, implying the onset of a region with constant shear stress. Just as important is the fact that the plateau region is bounded on the left and right by shear rates approximately corresponding to the inverse disengagement time and the inverse Rouse time, respectively. At this stage, we also investigated the effect of Δt and Δt_{ent} on the steady shear stress at high shear rates—the region characterized by large chain stretches. To examine this effect, we ran simulations with $\Delta t = \Delta t_{\mathrm{ent}} = 0.01$ and with $\Delta t = \Delta t_{\mathrm{ent}} = 0.02$. As seen in Figure 16, we find that the mean error for $\dot{\gamma}\tau_{\mathrm{R}}^{(\mathrm{m})} \geq 1$ is ~14% (a further discussion regarding the choice of entanglement release parameters is presented in section 4).

In Figure 17, we plot results for a system with $Z_0 = 15$. For these simulations, since we expect stiffer entanglement strands, we reduced the time step to 0.001 and set $\Delta t_{\mathrm{ent}} = 0.002$. Similar to the $Z_0 = 10$, system, we see the appearance of a stress plateau for intermediate flow rates and observe a rise in the stress beginning at $\dot{\gamma}\tau_{\mathrm{D}}^{(\mathrm{m})} \approx 8$, earlier than the expected value of $\dot{\gamma}\tau_{\mathrm{D}}^{(\mathrm{m})} = 45$ (i.e., where $\dot{\gamma}\tau_{\mathrm{R}}^{(\mathrm{m})} = 1$ for $Z_0 = 15$). This early rise in the stress indicates that even for $\dot{\gamma}\tau_{\mathrm{R}}^{(\mathrm{m})}$ slightly less than unity, significant stretching of entanglements is observed, in agreement with the large distributions of orientations and extensions that we reported in the previous section of this paper. It is also possible that our entangling procedure, chosen for computational speed, could account for the relatively early upturn in the shear stress and the variation of results with the chosen time step as seen in Figure 16. To investigate the effect of different entanglement procedures, we implemented the method proposed by Masubuchi et al.[20] and Yaoita et al.[21] The results from these simulation studies are presented later in this work.

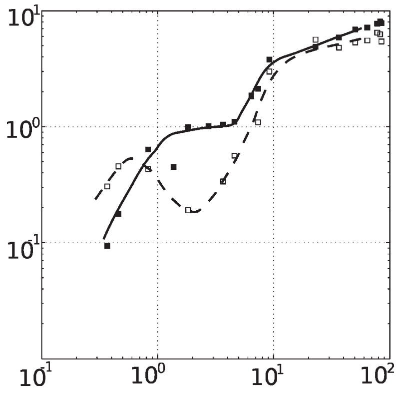

Figure 17. Shear stress (σ_{12}) vs shear rate ($\dot{\gamma}\tau_{\mathrm{D}}^{(\mathrm{m})}$) for $Z_0 = 15$. The filled symbols are simulations where constraint release events occur much more frequently than the open symbols. The stress data have been scaled such that the plateau occurs at unity. Lines to guide the eye are plotted as well.

Additional simulations at $Z_0 = 15$ were conducted, keeping all parameters constant except that Δt_{ent} was set to 0.02. This change results in a markedly different shear stress curve, shown by the open symbols in Figure 17. As mentioned previously, the reduction in constraint renewal frequency essentially diminishes the effects of CR. Thus, in the intermediate region, corresponding to the shear stress plateau, where CR is important, we see a significant decrease in stress. This aphysical behavior is exactly what was predicted by the original reptation-based theories that lacked constraint release. This result, obtained via direct simulation of an entangled network, unequivocally demonstrates that the renewal of constraints is the primary cause of the stress plateau and for the previously mentioned "frozen" orientation states. Even without CR, we note that at fast flows, where the behavior of this system is dominated by stretching, the stress curve quickly increases and asymptotes to the curve generated by systems inclusive of constraint release.

In the fast flow region, we observe a rise in the shear stress and find that $\sigma_{12} \sim \dot{\gamma}^{0.55}$, as predicted by theory. This is interesting because rheological measurements performed by Teixeira et al. on shorter λ-DNA chains showed a linear increase of shear stress with shear rate in this region.[19] This difference allude to a possible chain length dependent behavior of entangled systems under such strong flows.

To further evaluate the accuracy of our bulk simulation results, we used the experimental results published by Jary et al. for an entangled solution of T4-DNA,[35] a 166 kbp long strand of DNA with a molecular weight of 1.11×10^8 g/mol. To facilitate a comparison, we assume that T4-DNA is well described as a polymer with 700 Kuhn steps with a Kuhn length of 102.2 nm.[35,52] The experimental results for a concentration of 0.7 mg/mL DNA (corresponding to approximately 12−13 entanglements per chain) were compared with our simulations run at $Z_0 = 10$ (where the number of entanglements during the run fluctuate between 9 and 11). The normalized average stress versus strain rate curve (such

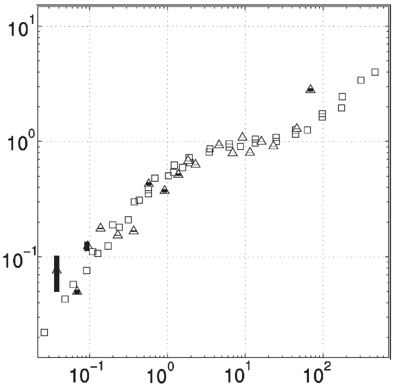

Figure 18. Comparison of shear stress vs strain rate. Simulation results (white triangles) were for $Z_0 = 10$, and experimental data (white squares) for T4-DNA were obtained from Jary et al. The *y*-axis for each curve is scaled such that the plateau stress value is unity, and on the *x*-axis we plot $\dot{\gamma}\tau_D^{(m)}$. The bars plotted for the simulation data are of size $\pm[Var(\sigma_{12}(t))]^{1/2}$ obtained via time traces are shown.

that the plateau has a value of unity) has been shown in Figure 18. The abscissae for the experimental results was scaled by an additional factor of 7.53 to account for the differences in polymer concentration (calculated using empirical scalings provided by Jary et al.).

Figure 18 shows that the simulations are able to achieve near-quantitative agreement with actual experimental results, including the initial rise of stress with shear rate followed by the onset of the plateau region and finally the upturn in the stress due to chain stretch. These indicators seen in Figure 18 reinforce the ability of this simulation technique to capture most of the salient features of entangled polymeric behavior not only qualitatively but also quantitatively.

To understand the simultaneous configurational changes that occur, we recorded $\langle \mathbf{X}_x \rangle$ and $\langle \mathbf{X}_y \rangle$, quantities closely related to the shear stress. These averages, plotted in Figures 19 and 20, show that for $\dot{\gamma} \sim (\tau_D^{(m)})^{-1}$ the sizes in either direction are only slightly perturbed from their zero flow rate limit. We might reasonably assume that the action of constraint release is able to prevent a drastic decrease in the size in the gradient direction and maintain nearly constant chain sizes. Proceeding toward the high flow rate side of the plateau, we start seeing increases in chain sizes in the flow direction. However, the contributions to the shear stress by the onset of stretch are counteracted by the decrease in the size of the chains in the gradient direction. A decrease in the projected size in the gradient direction causes the chains to present a smaller cross section in the flow direction and thus leads to a lower shear stress. Thus, a decrease in $\langle \mathbf{X}_y \rangle$ would contribute negatively to shear stresses. This careful balancing act between the sizes in the gradient and flow directions, which also results in the incomplete alignment of chains in the flow direction, seems to be the microstructural cause for the emergence of a constant shear stress portion in entangled polymer solutions. In terms of conventional nomenclature, this would be analogous to suggesting that the presence of near constant shear stress is due to the simultaneous decrease in the tube diameter and increase in the tube length, at rates corresponding to the stress plateau. At even higher flow strengths, the onset of chain stretch would cause the size in the flow direction to increase faster than the rate at which the size in the gradient direction decreases, resulting in the upturn in shear stress at fast shearing flow conditions. These simulations of varying shear stress with shear rate, including the presence of a shear stress plateau, are a good indication that our method is able to incorporate all the essential physics required to predict the physical rheological behavior of entangled polymer systems in shear.

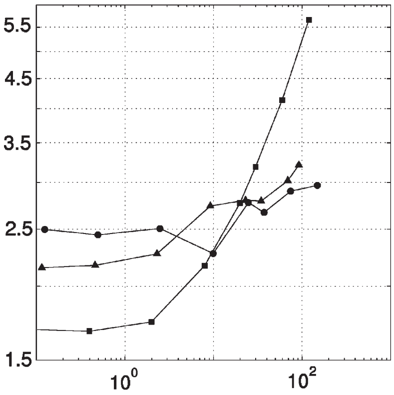

Figure 19. Changes in the average size of polymer chains in the flow direction as a function of $\dot{\gamma}\tau_D^{(m)}$. $Z_0 = 7$ (squares), $Z_0 = 10$ (triangles), and $Z_0 = 12$ (circles).

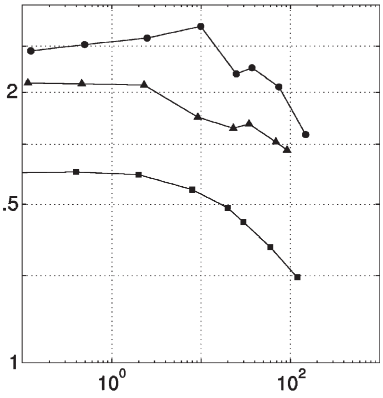

Figure 20. Changes in the average size of polymer chains in the gradient direction as a function of $\dot{\gamma}\tau_D^{(m)}$. $Z_0 = 7$ (squares), $Z_0 = 10$ (triangles), and $Z_0 = 12$ (circles).

3.7. Linear Viscoelasticity.

The linear viscoelastic (LVE) behavior of complex fluids is usually probed under conditions with small amplitude sinusoidally varying deformations of the form $\gamma = \gamma_0 \sin(\omega t)$, where the stress can be represented as

$$\sigma = \gamma_0[G' \sin(\omega t) + G'' \cos(\omega t)] \tag{13}$$

The relative values of the storage (G') and the loss (G'') moduli are indicative of the solid/liquid like nature of the fluid in question. Generally, for liquidlike substances where stresses can be quickly dissipated $G'' > G'$. In contrast, solidlike substances are able to store elastic energy, and so one observes $G' > G''$. However, most complex fluids display both solid and liquid behavior and thus manifest complicated storage and loss curves. Often, polymeric materials will display a characteristic frequency, ω_C, where the loss and storage moduli intersect. This crossover frequency represents the frequency when the material starts to become more solidlike and is commonly interpreted to be the inverse of the longest characteristic time scale of the system. For concentrated polymer solutions and melts, ω_C has usually considered to be the inverse of the disengagement time.

To measure the LVE properties via our simulations, the total shear stress was recorded at equilibrium and its autocovariance, $C(t)$, was calculated analogously to eq 8. The complex frequency-dependent viscosity was then estimated using[53]

$$[\eta(\omega)] = A \int_0^\infty \exp(-i\omega t) C(t)\, dt \tag{14}$$

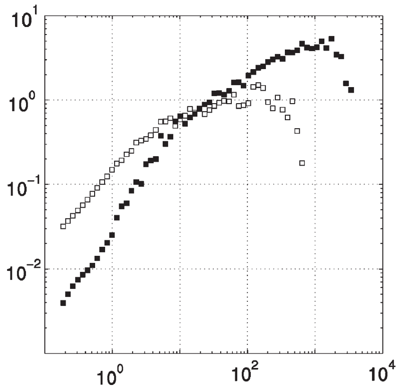

Figure 21. Loss (■) and storage (□) moduli for $Z_0 = 7$ plotted versus $\omega\tau_D^{(m)}$. The crossover frequency is ~10.

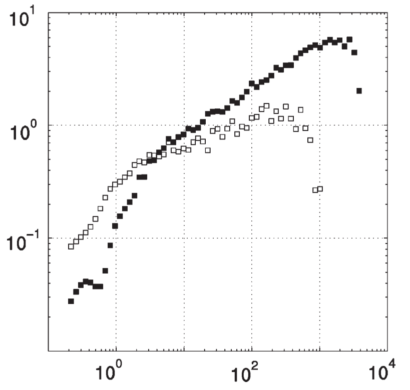

Figure 22. Loss (■) and storage (□) moduli for $Z_0 = 10$ plotted versus $\omega\tau_D^{(m)}$. The crossover frequency is ~5.

where the proportionality constant, A, is equal to $\zeta_n(6\eta_0 a)^{-1}$, when the complex viscosity is rendered dimensionless using the polymeric molecular weight as $M_w(N_A a^3)^{-1}$. Representing this viscosity as $\eta'(\omega) + i\eta''(\omega)$, the loss and storage moduli are extracted via the following relations:[54]

$$G'(\omega) = \omega\eta''(\omega) \tag{15}$$

$$G''(\omega) = -\omega\eta'(\omega) \tag{16}$$

In Figures 21–23, we present LVE results for $Z_0 = 7$, 10, and 15, respectively. Our results clearly show the variation in the behavior of the loss and storage moduli as we change the entanglement number. These results are qualitatively very similar to those obtained via rheometric measurements performed on λ-DNA solutions by Teixeira and co-workers to characterize the solutions used for single molecule experiments.[19] As in experiments, at low entanglement number, we notice that both the G' and G'' curves are relatively featureless and monotonically increase with frequency (the dropoff at high frequencies is an artifact of aliasing which arises when transforming a finite amount of time based data into the frequency domain). However, as Z_0 is raised, the storage modulus starts to develop a plateau and the loss modulus presents a dip at intermediate frequencies. Interestingly, at $Z_0 = 7$, the crossover frequency is not at its expected value of unity and actually $\omega_C \approx 10$. As the entanglement number is increased, we start to discern more separation between the loss and storage curves in the intermediate range of frequencies and also note that the crossover frequency migrates toward the left and at $Z_0 = 15$, $\omega_C \approx 2$. This highlights the fact that at low entanglement number the small separation between the Rouse and disengagement time results in all the microscale processes, such as length fluctuations, constraint renewal, etc., acting together and causing the longest relaxation time scale to differ from its theoretically predicted value. An important consequence of these findings is that setting the inverse of the crossover frequency equal to the disengagement time is correct only in the concentrated regime (i.e., where one can sufficiently differentiate the effects of reptation from other microscale effects) and not at low entanglement numbers.

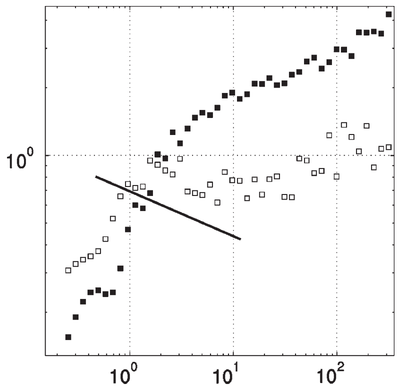

Figure 23. Loss (■) and storage (□) moduli for $Z_0 = 15$ plotted versus $\omega\tau_D^{(m)}$. The crossover frequency is ~2. The solid line is a curve with a slope of -0.2.

Regarding the shape of the loss modulus, at $Z_0 = 15$ we notice the presence of a dip at intermediate frequencies, a classic sign of entangled solution behavior. This decrease in G'' has been attributed to length fluctuations which aid the dissipation of energy by rapidly retracting and extending from the tube confining a polymer chain.[43,55] Within this region, it has been demonstrated that the addition of fluctuations changes the exponent from $-1/2$ (a result derived by including reptation and high-frequency Rouse modes) to $-1/4$. In extremely entangled cases (hundreds of entanglements per chain), a region of both $\omega^{-1/2}$ and $\omega^{-1/4}$ is seen in this intermediate region—the former arising due to reptation and high-frequency Rouse modes and the latter upon the inclusion of contour length fluctuations. In moderately entangled cases, such as for $Z_0 = 15$, as mentioned previously, the regions dominated by these various phenomena are not well demarcated, and thus one cannot reproduce the loss modulus curve described above. Furthermore, the addition of constraint release changes the shape of the loss curve by smoothening out the local peak and raising the loss minima.[55] In these cases, the dip has been shown to be less severe and decays with a slope of less than $-1/4$.[43,55] In accordance with this expectation, the loss modulus for $Z_0 = 15$ displays a slope of approximately -0.2.

4. Comparison with Recently Proposed Constraint Renewal Procedure

In this section we study the effect of a new constraint renewal procedure on the simulation results and also compare the results with experimental data for larger entanglement numbers. We have used a simulation technique recently proposed by Yaoita et al.,[21] which is a modified version of the original implementation by Masubuchi et al.[20] The salient features of the refined version are (i) a new constraint renewal mechanism, (ii) variable subchain friction coefficient, and (iii) an explicit time stepping scheme. The new constraint renewal mechanism is used to create new entanglements with the same monomer density as that found at equilibrium. Thus, it maintains the equilibrium of chain ends

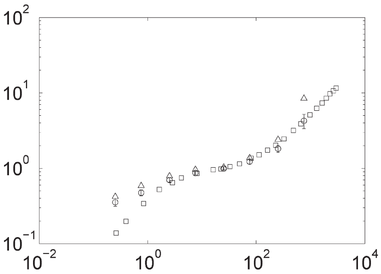

Figure 24. Plot of normalized shear stress vs $\dot{\gamma}\tau_D$. Comparison of the simulation technique of Yaoita et al.[21] for $Z_0 = 10$ with experimental data obtained for T4-DNA by Jary et al.[35] Squares denote experimentally measured values; circles and triangles represent simulation results obtained using $\Delta t_{ent} = 0.4 = 400\Delta t$ and $\Delta t_{ent} = 1.0 = 1000\Delta t$, respectively.

which is different from the previous mechanism where some artificial stretch was introduced upon hooking. This reduces the variation in the measured stress when an entanglement is created or destroyed. The friction coefficients of the subchains are chosen to reflect the variable number of monomers they contain, different from the method implemented previously in this work (which had a fixed friction for subchain). This change seems suitable for nonequilibrium dynamics where the number of monomers can differ significantly from one subchain to other. Finally, instead of using an implicit scheme, as in previous simulations, we use an explicit time stepping here.

The governing equations for node and monomer dynamics remain the same as before. However, to account for variable resistivity, the friction coefficient ζ for a node is given by

$$\zeta = \zeta_m \sum_{\alpha=1}^{N_c} n_\alpha/2 \tag{17}$$

The sliding friction coefficient ζ_s is taken as the average of the friction coefficients associated with the two adjacent entanglement strands.[21]

$$\zeta_s = \zeta_m \frac{n_{\alpha+1}+n_\alpha}{2} \tag{18}$$

where ζ_m is the friction coefficient of a Kuhn segment.

As in the simulations of Yaoita et al.,[21] we use explicit Euler time stepping to evolve the dynamics in time. The effect of time step size on the dynamics was studied, and the results were found to be insensitive to time step sizes $\Delta t \leq 0.01$. The simulations reported here were performed at $\Delta t = 0.001$.

As discussed before, in addition to the node and monomer dynamics, constraint renewal/release mechanisms account for topological changes in the entangled chain network. These mechanisms occur on the order of Rouse time, which is consistent with the coarse graining of the model, and result in the formation/destruction of entanglements. The frequency of these topological changes is governed by the relaxation time of the chain ends, which is assumed to be equal to the Rouse time of a tethered chain ($\Delta t_{ent} = 0.4 = 400\Delta t$). So a search for a suitable partner is made within a unit radius (i.e., nondimensionalized equilibrium distance between entanglements a) at a regular time interval of Δt_{ent}.[21] If a suitable partner is found, then an entanglement is created without violating the maximum extensibility and conserving the number of Kuhn steps per chain. This is different from the procedure outlined previously in the Model Description section.

The simulations are performed for $Z_0 = 10$, 15, and 25. In Figures 24−26, simulation results are compared to that of Jary's experimental data.[35] The experimental results for concentrations of 0.49, 0.7, and 1.05 mg/mL are compared with simulation results corresponding to $Z_0 = 10$, 15, and 25. The y-axis for each curve was scaled such that the plateau stress value was unity, and on the x-axis we plot $\dot{\gamma}\tau_D$. Error estimates are presented via error bars of size $\pm Var(\sigma_{xy})$ obtained via time traces. The simulation results were further shifted to account for variation in concentration. The simulations clearly capture the shear stress plateau for both the entanglement numbers. The comparison for larger entanglement numbers is better, and we do not observe a flattening of the shear stress at low strain rates. Also, to study the effect of constraint renewal frequency on the simulation results, we ran simulations for $\Delta t_{ent} = 400\Delta t$ and $\Delta t_{ent} = 1000\Delta t$. There is a small deviation between the two plots. Nevertheless, as can see both the simulation methods (Yaoita et al.'s and the method presented in the previous sections) are able to capture experimentally observed variations in the bulk stresses of polymer solutions. As discussed below, we see a drop in entanglement number as the shear rate is increased. Hence, here we use the concentration of 0.49 mg/mL (corresponding to 6−9 entanglements per chain) to compare to our simulation results for $Z_0 = 10$. Previously in Figure 18, we used Jary's 0.7 mg/mL concentration data (corresponding to 12−13 entanglements per chain) to compare to our $Z_0 = 10$ data as the variation in entanglement number was not significant since that process of constraint renewal/release was able to maintain a nearly constant entanglement number.

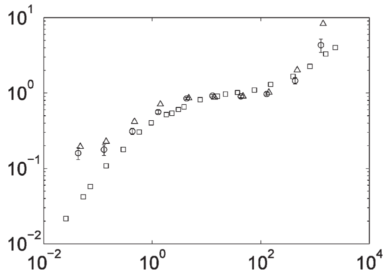

Figure 25. Plot of normalized shear stress vs $\dot{\gamma}\tau_D$. Comparison of the simulation technique of Yaoita et al.[21] for $Z_0 = 15$ with experimental data obtained for T4-DNA by Jary et al.[35] Squares denote experimentally measured values; circles and triangles represent simulation results obtained using $\Delta t_{ent} = 0.4 = 400\Delta t$ and $\Delta t_{ent} = 1.0 = 1000\Delta t$, respectively.

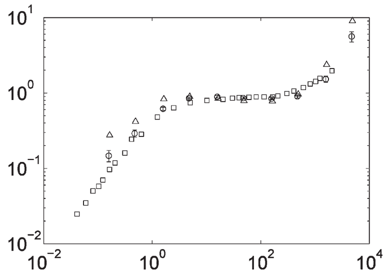

Figure 26. Plot of normalized shear stress vs $\dot{\gamma}\tau_D$. Comparison of the simulation technique of Yaoita et al.[21] for $Z_0 = 25$ with experimental data obtained for T4-DNA by Jary et al.[35] Squares denote experimentally measured values; circles and triangles represent simulation results obtained using $\Delta t_{ent} = 0.4 = 400\Delta t$ and $\Delta t_{ent} = 1.0 = 1000\Delta t$, respectively.

In Figure 27, we compare the variation of shear stress with Peclet number ($\dot{\gamma}\tau$), where τ, the Rouse time for an entanglement strand, is the unit of time. As reported by Jary, we also observe a good superposition of the three curves for the highest shear rates. This indicates that for high shear rates ($\dot{\gamma}\tau_R \sim O(1)$) the normalized shear stress has a very weak dependence on chain length

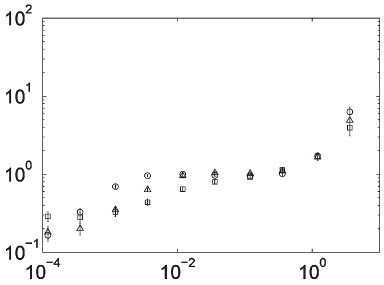

Figure 27. Plot of normalized shear stress vs Peclet number ($\dot{\gamma}\tau$). Squares, triangles, and circles represent simulation results obtained for $Z_0 = 10$, 15, and 25, respectively, using $\Delta t_{\mathrm{ent}} = 0.4 = 400\Delta t$.

(or the number of entanglements), and the stress is mainly due to stretched subchains. Furthermore, we also see a large variability in configuration for various shear rates, in accordance with the results presented previously in this work. As reported by Yaoita, a decrease in entanglement number as shear rate is increased was witnessed in our simulations. The drop in the number of entanglements is significant, and this shear-induced disentanglement is greater for long chains. Entanglements decreased by 60−70% for the largest shear rate and the longest chain ($Z_0 = 25$).

Note in Figure 25 this simulation procedure reproduces the complete shear stress plateau for $Z_0 = 15$, as compared to the previous implicit simulation result where we obtained an earlier rise in shear stress resulting in a smaller plateau. However, the significant drop in entanglement number for high flow rates limits the range of accessible shear rates and also raises some important questions about the dynamics of entangled DNA at high shear rates. Additionally, some inadequacies, i.e. time step sensitivity, have also been reported for extensional flows at high flow rates.[21] We believe that a semi-implicit algorithm of the form presented earlier in this paper would be helpful in resolving this issue, which is mainly due to the limitation of an explicit time stepping scheme in resolving the high-frequency dynamics of highly stretched chains in fast extensional flows.

5. Conclusions

In this work, we have developed a simulation for entangled wormlike polymer chains in shear flows. We have successfully incorporated finitely extensible chains in a periodic homogeneous system with real space coupling. Our model also contains monomer motion along a chain's backbone and thus inherently contains chain-end fluctuations. Constraint release events are driven by the reptative motion of the chain which can significantly be affected by the ambient system conditions, such as flow.

Using this methodology, we have obtained a scaling of $\tau_{\mathrm{D}}^{(\mathrm{m})} \sim Z^{3.4}$, which is the experimentally measured relation for the longest relaxation time with entanglement number. Using time traces, we demonstrate the existence of a variety of conformational dynamics adopted by individual chains, including cases where polymers tumble over the course of one disengagement time. Such rotational fluctuations have also been observed by others using molecular dynamics simulations at much higher flow strengths.[45] We also obtain relations for the power spectrum of length fluctuations of concentrated chains. We find that $S(\omega) \sim \omega^{-m}$, where m varies from approximately 1.6 to 2 from equilibrium to strong flow conditions. This is indicative of the diminishing contribution from high-frequency modes as the chains start to stretch. With regards to chain statistics, we find a significantly broad distribution in chain size and orientation for a variety of flow strengths—possibly invalidating the use of preaveraging approximations that might be invoked in other models. These results are in agreement with single molecule data for λ-DNA, and the orientational variation seen in our simulations corresponds well to previously observed nonlinear orientational behavior in birefringence measurements. Finally, we also obtain good agreement with experiments (T4-DNA) with respect to the shear stress vs rate curve which contains a plateau in the intermediate region. Within this plateau region, we also notice variations in chain sizes in the flow and gradient planes, a balance of which could explain the existence of a stress plateau. By varying the frequency of constraint release events in our simulations, we are able to show that the absence of constraint release leads to significant shear thinning in the plateau region, and thus it is this same constraint release phenomenon that gives rise to the plateau and "frozen" orientations observed in our simulations. The linear viscoelasticity predictions of our experiments suggest that setting the crossover frequency equal to the inverse of the disengagement time, at low entanglement number, might lead to incorrect results due to the small separations between the disengagement and Rouse time scales. At larger number of entanglements, our simulations are also able to predict a dip in the loss modulus at intermediate frequencies. The existence of a stress plateau and a dip in the loss modulus are classic signs of entangled polymer systems. Finally, we find that our simulation method and that of Yaoita et al.[21] are both able to reproduce the experimentally measured shear stress for concentrated solutions of T4-DNA, and both simulation methods display large variations in chain configuration over a range of shear rates comparable to the inverse disengagement time.

Acknowledgment. This work was supported by a grant from the Materials Research Science and Engineering Center Program of the National Science Foundation (NSF) under DMR 9808677.

References and Notes

(1) Rouse, P., Jr. *J. Chem. Phys.* **1953**, *21*, 1272.
(2) Zimm, B. *J. Chem. Phys.* **1955**, *24*, 269.
(3) Doi, M.; Edwards, S. Oxford University Press: Oxford, UK, 1986.
(4) Marrucci, G.; Ianniruberto, G. *Philos. Trans. Math. Phys. Eng. Sci.* **2003**, *361*, 677–688.
(5) Mead, D.; Larson, R.; Doi, M. *Macromolecules* **1998**, *31*, 7895–7914.
(6) Graessley, W. *Adv. Polym. Sci.* **1982**, *47*, 67–117.
(7) Viovy, J.; Monnerie, L.; Tassin, J. *J. Polym. Sci., Polym. Phys. Ed.* **1983**, *21*, 2427–2444.
(8) Marrucci, G. *J. Non-Newtonian Fluid Mech.* **1996**, *62*, 279–289.
(9) Milner, S.; McLeish, T.; Likhtman, A. *J. Rheol.* **2001**, *45*, 539.
(10) Graham, R.; Likhtman, A.; McLeish, T.; Milner, S. *J. Rheol.* **2003**, *47*, 1171.
(11) Baumgärtner, A.; Binder, K. *J. Chem. Phys.* **1981**, *75*, 2994.
(12) Kremer, K.; Grest, G. *J. Chem. Phys.* **1990**, *92*, 5057.
(13) Nikunen, P.; Vattulainen, I.; Karttunen, M. *Phys. Rev. E* **2007**, *75*, 36713.
(14) Squires, T.; Quake, S. *Rev. Mod. Phys.* **2005**, *77*, 977–1026.
(15) Jung, B.; Bharadwaj, R.; Santiago, J. *Anal. Chem.* **2006**, *78*, 2319–2327.
(16) Stoltz, C.; de Pablo, J.; Graham, M. *J. Rheol.* **2006**, *50*, 137.
(17) Schieber, J.; Nair, D.; Kitkrailard, T. *J. Rheol.* **2007**, *51*, 1111.
(18) Perkins, T.; Smith, D.; Chu, S. *Science* **1994**, *264*, 819.
(19) Teixeira, R.; Dambal, A.; Richter, D.; Shaqfeh, E.; Chu, S. *Macromolecules* **2007**, *40*, 2461–2476.
(20) Masubuchi, Y.; Takimoto, J.; Koyama, K.; Ianniruberto, G.; Marrucci, G.; Greco, F. *J. Chem. Phys.* **2001**, *115*, 4387.
(21) Yaoita, T.; Isaki, T.; Masubuchi, H., Y.; Watanabe; Ianniruberto, G.; Greco, F.; Marrucci, G. *J. Chem. Phys.* **2008**, *128*, 4387.
(22) Rakshit, A.; Picu, R. *J. Chem. Phys.* **2006**, *125*, 164907.
(23) Padding, J.; Briels, W. *J. Chem. Phys.* **2002**, *117*, 925.
(24) Padding, J.; Briels, W. *J. Chem. Phys.* **2003**, *118*, 10276.
(25) Masubuchi, Y.; Ianniruberto, G.; Greco, F.; Marrucci, G. *Modell. Simul. Mater. Sci. Eng.* **2004**, *12*, S91–S100.
(26) Bustamante, C.; Marko, J.; Siggia, E.; Smith, S. *Science* **1994**, *265*, 1599–1600.
(27) Larson, R. *Appl. Rheol.* **2000**.
(28) Rubinstein, M.; Colby, R. *Polymer Physics*; Oxford University Press: New York, 2003.

(29) Tao, H.; Huang, C.; Lodge, T. *Macromolecules* **1999**, *32*, 1212–1217.

(30) Even though λ-DNA is well approximated as a polymer chain with 150 Kuhn steps, its persistence length is sensitive to experimental conditions such as temperature, salt concentrations, etc. Furthermore, simulations have shown that the behavior of a 220 Kuhn step chain in steady shear is quantitatively the same as that of a 150 Kuhn step chain. Due to this variability, we choose to assume a value of 200 for λ-DNA which corresponds to T4-DNA (3.4 times longer than λ-DNA) having about 685 Kuhn steps.

(31) Nair, D.; Schieber, J. *Macromolecules* **2006**, *39*, 3386–3397.

(32) Allen, M.; Tildesley, D. *Computer Simulation of Liquids*; Oxford University Press: Oxford, U.K., 1989.

(33) Bhattacharjee, P.; Nguyen, D.; McKinley, G.; Sridhar, T. *J. Rheol.* **2002**, *47*, 269.

(34) Islam, M.; Archer, L. *J. Polym. Sci., Part B: Polym. Phys.* **2001**, *39*, 2275–2289.

(35) Jary, D.; Sikorav, J.; Lairez, D. *Europhys. Lett.* **1999**, *46*, 251–255.

(36) Mason, T.; Dhople, A.; Wirtz, D. *Macromolecules* **1998**, *31*, 3600–3603.

(37) Kasehagen, L.; Macosko, C. *J. Rheol.* **1998**, *42*, 1303.

(38) Pattamaprom, C.; Larson, R.; Van Dyke, T. *Rheol. Acta* **2000**, *39*, 517–531.

(39) Rubinstein, M.; Colby, R. *J. Chem. Phys.* **1988**, *89*, 5291.

(40) Teixeira, R. E. Ph.D. Thesis, Stanford University, **2005**.

(41) Boukany, P.; Hu, Y.; Wang, S. *Macromolecules* **2008**, *41*, 2644–2650.

(42) Doi, M. *J. Polym. Sci., Polym. Phys. Ed.* **1983**, *21*, 667–684.

(43) Milner, S.; McLeish, T. *Phys. Rev. Lett.* **1998**, *81*, 725–728.

(44) Schroeder, C.; Teixeira, R.; Shaqfeh, E.; Chu, S. *Phys. Rev. Lett.* **2005**, *95*, 18301.

(45) Kim, J. M.; Edwards, B. J.; Keffer, D. J.; Khomami, B., submitted to *Phys. Lett. A*.

(46) Shumway, R.; Stoffer, D. *Time Series Analysis and Its Applications*; Springer: Berlin, 2000.

(47) Hur, J.; Shaqfeh, E.; Larson, R. *J. Rheol.* **2000**, *44*, 713.

(48) These PSDs were extracted using the projected size in the flow direction rather than the end-to-end vector. Since the actual ends of the polymer chain are impossible to ascertain, one must resort to looking at the maximum size in a given direction instead. This difference is not expected to affect any scaling.[40]

(49) Schroeder, C.; Shaqfeh, E.; Chu, S. *Macromolecules* **2004**, *37*, 9242–9256.

(50) Mhetar, V.; Archer, L. *J. Polym. Sci., Part B: Polym. Phys.* **2000**, *38*, 222–233.

(51) Milner, S.; McLeish, T.; Likhtman, A. *J. Rheol.* **2001**, *45*, 539.

(52) Shaqfeh, E. *J. Non-Newtonian Fluid Mech.* **2005**, *130*, 1–28.

(53) Bixon, M. *Annu. Rev. Phys. Chem.* **1976**, *27*, 65–84.

(54) Diaz, F.; Garcia de la Torre, J. *Macromolecules* **1994**, *27*, 5371–5376.

(55) Likhtman, A.; McLeish, T. *Macromolecules* **2002**, *35*, 6332–6343. Hur, J.; Shaqfeh, E.; Babcock, H.; Smith, D.; Chu, S. *J. Rheol.* **2001**, *45*, 421.